A STUDY OF PHYSICAL MECHANISMS FOR FILAMENT ERUPTION AND CORONAL MASS EJECTION VIA NUMERICAL SIMULATION

A Progress Report for NAGW-9

Period of Performance: January 1, 1992 - December 31, 1992

S. T. Wu
Center for Space Plasma and Aeronomic Research
and Department of Mechanical Engineering
The University of Alabama in Huntsville

for
National Aeronautics and Space Administration
Headquarters
Washington, DC 20546

1 Introduction

During this period of performance (January 1, 1992 - December 31, 1992) we have accomplished the investigation of the following tasks:

a. Application of the Non-linear Force-free Field (NLFF) Model to study the active region evolution.

b. Coronal dynamical responses due to emerging flux including the transition region.

c. Loss of MHD equilibrium due to footpoint motions.

d. Two-dimensional MHD global coronal model: steady-state streamers.

The detailed description of these studies are included in the following sections:

2 Applications of the Non-Linear Force-Free Field (NLFF) Model to Study the Active Region Evolution

Since the publication of the first version of our extrapolation scheme (Wu et al. 1990), called "Progressive Extension Method (PEM)", further modification was made on the regularization-like technique. This new regularization-like technique can be summarized as follows: the expression for averaging given by Eqs. (3.5) and (3.6) of the paper by Wu *et al.* 1990 is modified as follows:

The regularization-like solution for the magnetic field vector, $\bar{B}'_{i,j}$ becomes

$$\bar{B}'_{i,j} = (1-\gamma)B_{i,j} + \gamma\bar{B}_{i,j} \tag{1}$$

where $\bar{B}_{i,j}$ is the same as Eq. (3.5) from the Wu *et al.* (1990) paper and

$$\gamma(z) = \gamma_0 exp[a(z/z_{max})] \tag{2}$$

with γ_0 being arbitrary and to be determined by a trial and error method until the solution converges and

$$a = ln(\gamma(z_{max})/\gamma_0) \tag{3}$$

By setting our goals on $\gamma(z_{max})$ and γ_0, a is determined.

Using this modified technique, we performed a number of significant tests by using a complicated analytical nonlinear force-free solution (Low and Lou, 1990) as the input to the numerical model. Figure 1 shows a top view of the field lines generated by: (a) an analytical solution (Low and Lou, 1990), and (b) a numerical solution obtained from extrapolation. Figure 2 shows three-dimensional field lines corresponding to the solutions given in Figure 1. **These results clearly demonstrate that the PEM (Wu *et al.* 1990) is a reasonable method to obtain nonlinear force-free fields by using vector field data in the photosphere.** The accuracy of the extrapolation can be shown as a function of height. It is recognized from these results that the height of the extrapolation is about one tenth of the horizontal boundary which is typically about 30,000 - 50,000 km.

We then applied this NLFF model to extrapolate the magnetic field configuration using the *measured* photospheric vector field at Beijing Observatory on 1989 March 9 and 11 to demonstrate the capability of this model. In order to show the validity of this NLFF model, we also show the computed potential field using the present algorithm to compare with the Schmidt's potential field model. This result is shown in Figure 3 (for 1989 March 10 at 0600 UT) which indicates that the results obtained from the present algorithm are identical to the classical Schmidt's model.

Figure 4 shows the nonlinear force-free extrapolation for 1989 March 10 (0600 UT) and 11 (0226 UT) respectively. From these results, we notice that, (i) the differences between the potential field and the NLFF models are significant. That is, the magnetic field structure represented by the NLFF model is believed to more closely resemble the realistic situation as shown in Figure 5. We clearly notice from Figure 5 that the loop structures revealed by the NLFF model closely resembled the H-α observations which the potential field model cannot show.

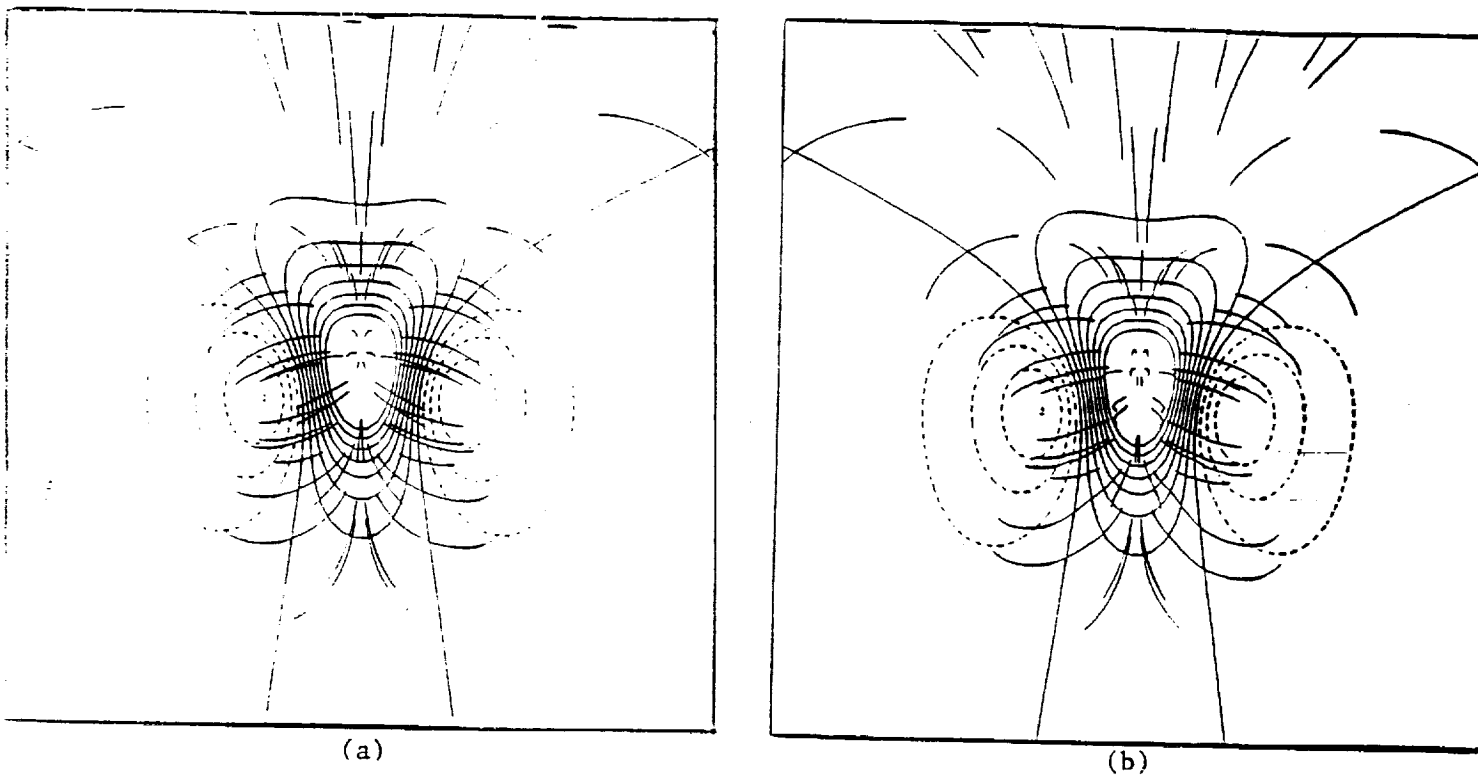

Figure 1: Comparison between (a) the analytical solution and (b) extrapolated solution using analytical data (i.e. data generated by solution given in (a)).

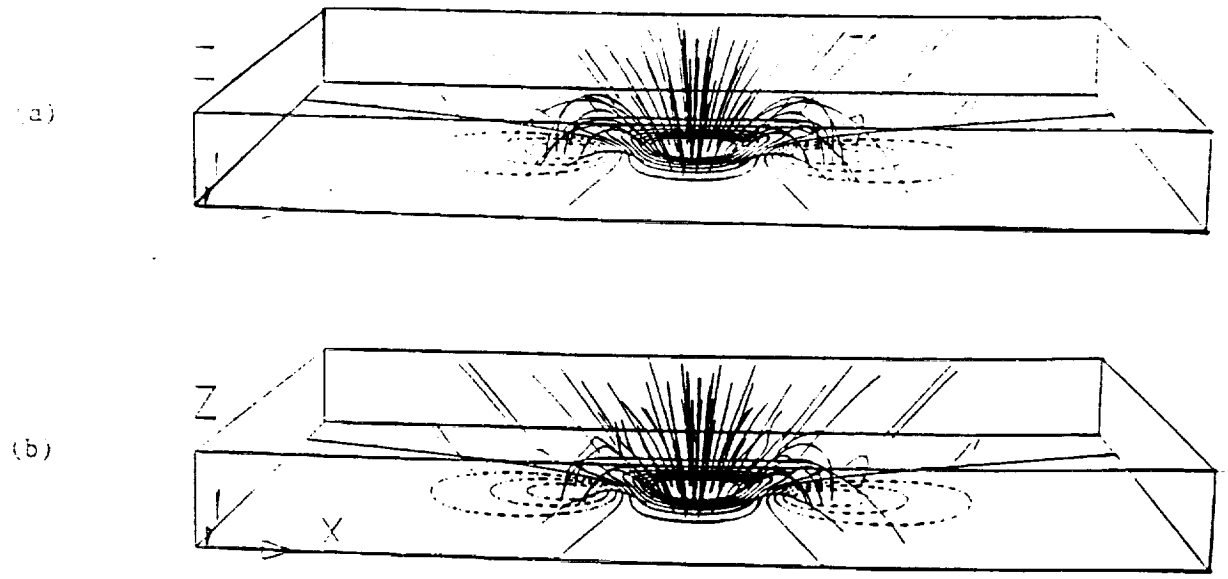

Figure 2: Three-dimensional representation of field lines obtained by analytical solution (a) and numerical model (b) corresponding to the solution given in Figure 1

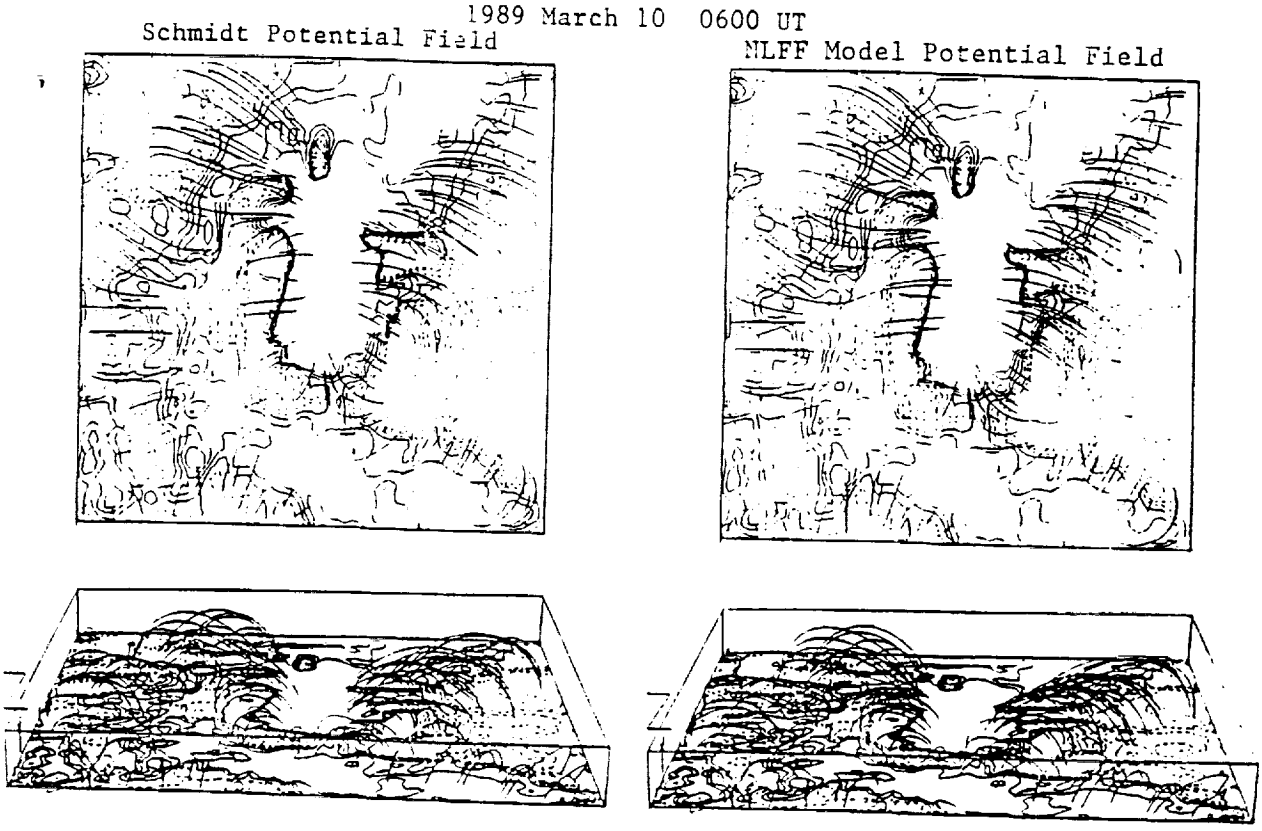

Figure 3: Comparison of NLFF Model and Potential solutions. Photospheric vector magnetograph measurements are shown by the solid (outward) and dashed (inward polarity) contours.

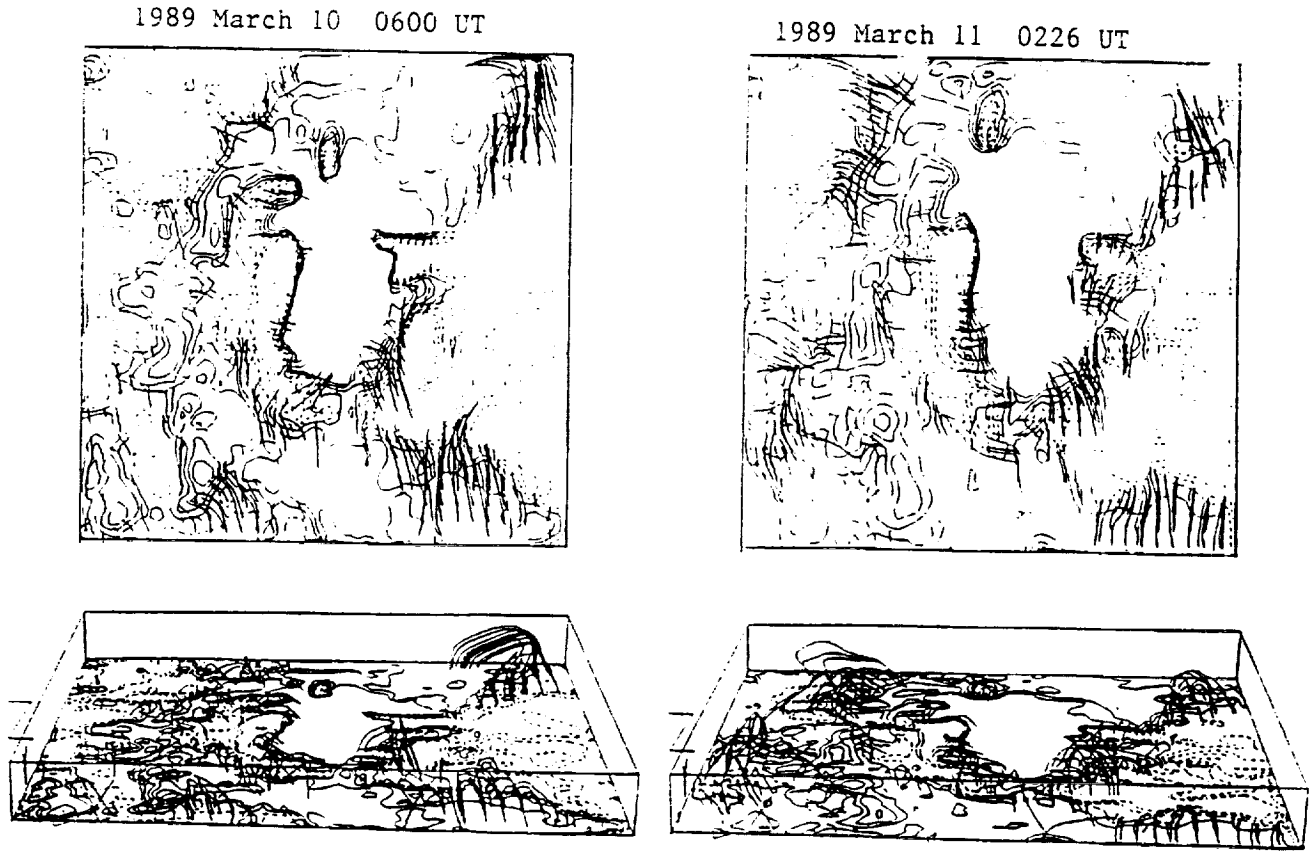

Figure 4: Simulated temporal evolution of NLFF Model solution over a period of about 20 hours. The dashed and solid contours are the photospheric vector magnetograph measurements.

3 Coronal Dynamical Responses Due to Emerging Flux Including the Transition Region

From the observations, it is inferred that the additional magnetic energy stored in the solar atmosphere very likely results from flux emergence from the sub-photospheric layer. It is difficult to model this physics because the characteristics of this part of the solar atmosphere (i.e. photosphere/chromosphere, transition region and corona) have several order-of-magnitude variations in density, pressure and plasma beta (i.e. $\beta = (\frac{16\pi nkT}{B^2})$), hence little progress has been made up to now. Recently, Wu *et al.* (1992) developed a self-consistent MHD model to address this problem. A more realistic energy equation was used in order to construct this model. This energy equation, which includes wave heating, radiative cooling, thermal conduction and joule heating, is given as:

$$\frac{\partial p}{\partial t} + (\vec{V} \cdot \nabla)p + \gamma p(\nabla \cdot \vec{V} + (\gamma - 1)(\nabla \cdot \vec{Q} - \frac{J^2}{\sigma} - G_{mech} + L_{rad}) = 0 \quad (4)$$

where, p = pressure, $\vec{V}$ = plasma flow velocity vector, $\vec{Q}$ = thermal conduction, J = electric current, G_{mech} = wave heating, L_{rad} = radiative cooling, γ = specific heat ratio and σ = electrical conductivity.

The other equations (i.e. continuity, momentum and the Maxwell equations) are identical to those used before (Wu *et al.* 1983b). The numerical method used for this study is the modified ICED-ALE (Implicit-Continuous-Eulerian-Difference-Mesh-Arbitrary-Lagrangian-Eulerian) method given by Wu *et al.* (1991b). The reason for choosing this method is because the Eulerian difference scheme usually used has a limitation on the grid size which becomes impractical when the spatial gradient becomes too large. A brief description of the numerical results obtained from this model is given as follows: Figure 6 shows the steady-state density, temperature, pressure and plasma beta distribution from the surface through the temperature minimum up to the lower corona ($\sim$ 3500 km) together with grid distribution at 50 s after introduction of emerging magnetic flux. These results are equivalent to the empirical model of the Harvard-Smithsonian model. Our next objective was to demonstrate that this model can be used to study the momentum and energy transport from the solar interior to the corona and thereby, to investigate the physical mechanism of coronal heating and solar wind acceleration. To accomplish this objective we introduced an emerging flux at the lower boundary and computed the evolutionary state of the plasma properties, velocity and magnetic field. The initial state is shown in Figure 6. Figures 7 and 8 show the evolutionary results for velocity, temperature, density, pressure, and magnetic field lines at time 500 s and 1000, after introduction of emerging flux. From these preliminary results, we found the following features (i.e. a paper is currently in preparation and the results were presented at the AAS/SPD Meeting June 6-11, 1992):

i. The emerging flux leads to the formation of a current sheet at the interface of the old and new magnetic fields and to its propagation upward toward the corona;

ii. The induced plasma flow oscillates vertically at the Brunt-Vaisala frequency with a period of 240 s.;

iii. Also, we showed that there is no oscillation when the gravity (unrealistically) is ignored.;

iv. The maximum downward flow ($\sim 20 kms^{-1}$) occurs in the neighborhood of the legs of the magnetic loop which is a typically observed feature.

4 Loss of MHD Equilibrium Due to Footpoint Motions: A Three-Dimensional, Time-Dependent MHD Simulation Model

Recently Sudan (1991) has demonstrated the phenomena of "loss of equilibrium" by using a set of reduced incompressible MHD equations. We have used a newly developed three-dimensional, time-dependent, compressible MHD simulation model (Sun and Wu, 1992) to demonstrate similar results. Parker (1972, 1981), in a long series of papers spanning almost two decades, has claimed that the coronal magnetic field, evolving in response to smooth continuous photospheric footpoint motions, will not be able to achieve a smooth, force-force equilibrium; instead, the field develops tangential discontinuties. It has been thought that these

Potential Fields at 15 March 1989 0151 UT

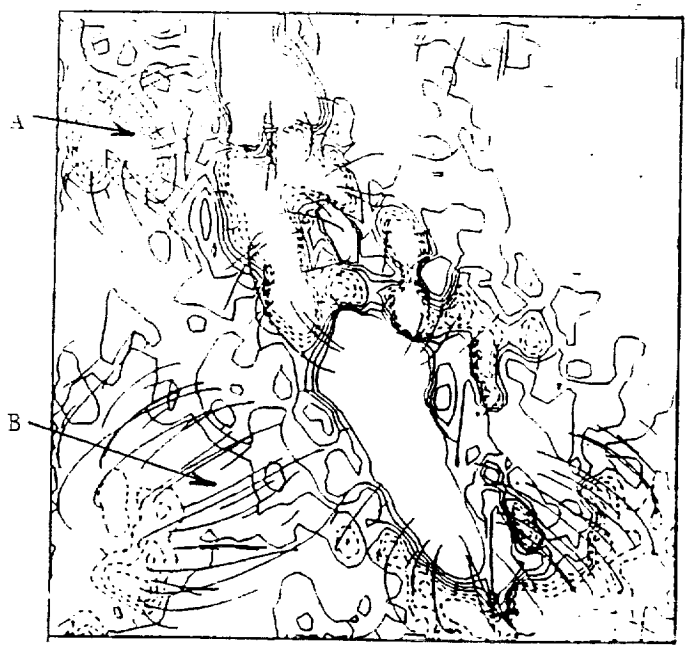

Figure 5. Comparison between the magnetic loop structures seen by H-α filtergrams and magnetic loops derived by the NLFF model as well as the potential field model: (a) the magnetic fields structure derived by the model at 1989 March 15 at 0315 UT overlay on the H-α picture. (b) the magnetic fields structure derived by the potential field model at 1989 March 15 at 0315 UT. Note the regions indicated by A and B. It is easy to recognize that the potential field model failed to match the H-α picture

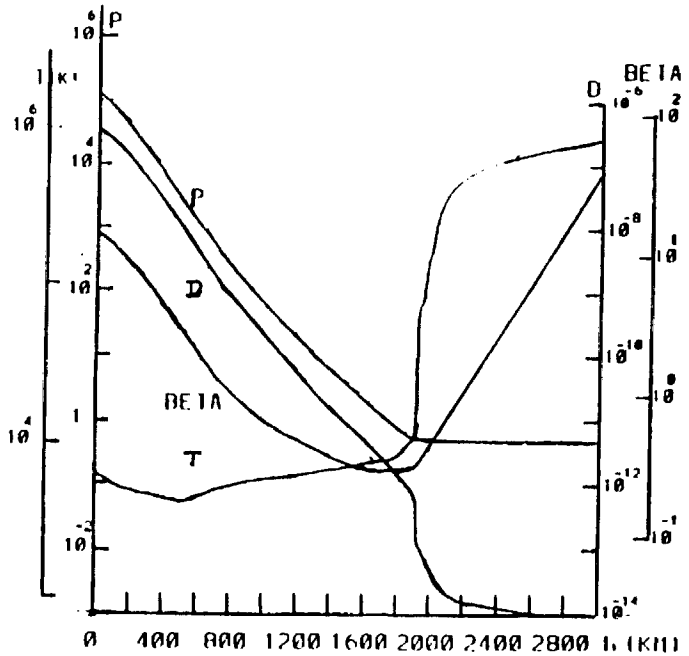

(a)

(b)

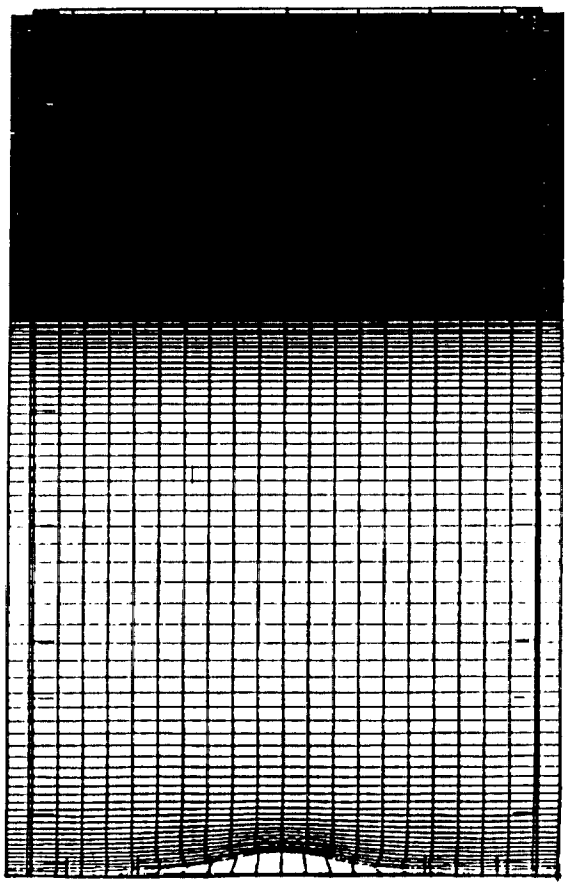

Figure 6. (a) Initial steady state of plasma p_o, ρ_o, T_o, $\beta(= p/(B^2/8\pi))$, in solar atmosphere. (b) Lagrangian network at t = 50 sec.

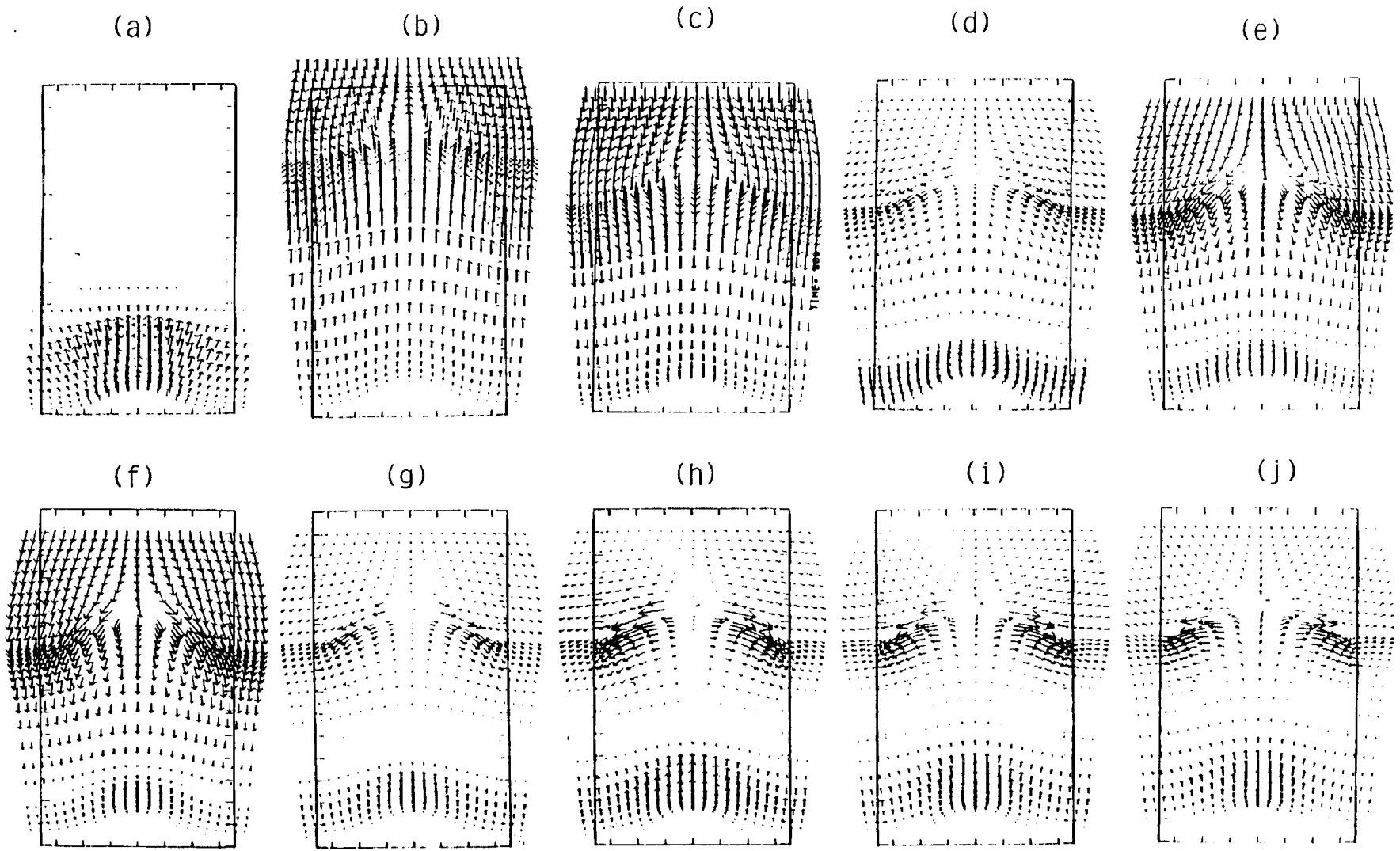

Figure 7. Evolution of plasma flow (velocity vectors). (a) at t = 100 sec. (b) at t = 200 sec. (c) at t = 300 sec. (d) at t = 400 sec. (e) at t = 500 sec. (f) at t = 600 sec. (g) at t = 700 sec. (h) at t = 800 sec. (i) at t = 900 sec. (j) at t = 1000 sec.

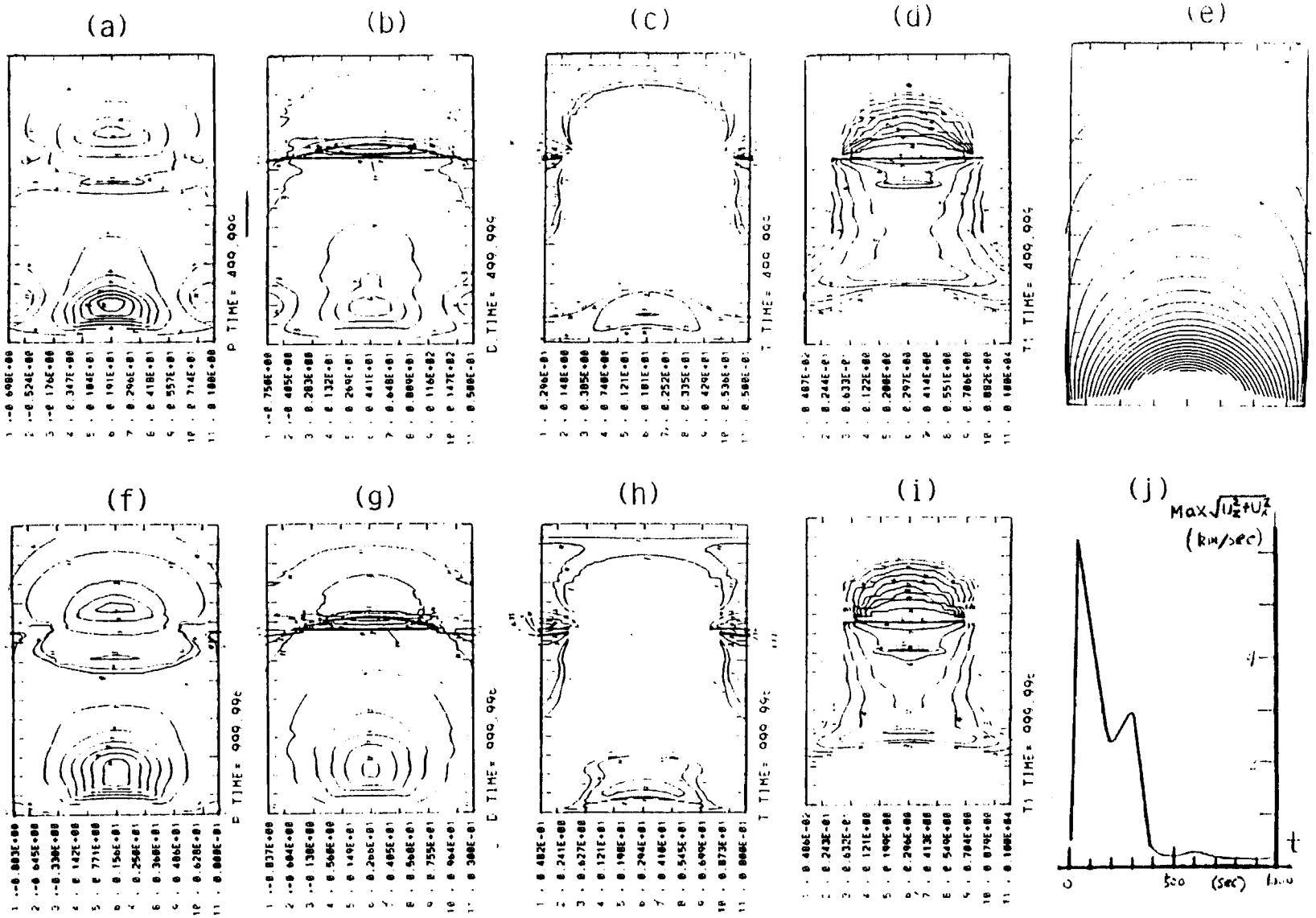

Figure 8. (a) $(p - p_o)/P_o$ contour at t = 500 sec. (b) $(\rho - \rho_o)/\rho_o$ contour at t = 500 sec. (c) $(T - T_o)/T_o$ positive temperature contour at t = 500 sec showing the regions with temperature rising. (d) $-(T - T_o)/T_o$ negative temperature contour at t = 500 sec. showing the regions with temperature decreasing (e) field lines at t = 1000 sec., indicating the new emerging field at the bottom boundary. (f) $(p - p_o)/p_o$ contour at t = 1000 sec. (g) $(\rho - \rho_o)/\rho_o$ contour at t = 1000 sec. (h) $(T - T_o)/T_o$ positive temperature contour at t = 1000 sec. (i) $-(T - T_o)/T_o$ negative temperature contour at t = 1000 sec. (j) Evolution of the maximum magnitude of velocities $MAX(\sqrt{(U_z^2 + U_x^2)_{i,j}})$.

discontinuties could lead to enhanced dissipation in current sheets and, moreover, could provide the energy release responsible for coronal heating (i.e. x-ray emissions as observed).

Our simulation for the loss of MHD equilibrium due to footpoint motion is based on a three-dimensional, time-dependent, compressible MHD model using a new NICE (Nimble Implicit-Continuous-Eulerian) scheme (Sun, 1991; Sun and Wu, 1992). The results of the simulation shown in Figure 9 are explained as follows: The sequence of panels, with projected field lines onto the x-z plane, shows that, up to about t_{max} (this "maximum time" is deduced from an analytical solution when the force-free solution reaches the critical state), the numerical results closely follow the analytical equilibrium sequence. After (t_{max}) the field lines start to oscillate with a maximum velocity reaching an amplitude of about $50 kms^{-1}$. This result suggests that "loss of equilibrium" has occurred. Since we are using the ideal MHD equations, no reconnection can take place, and an eruption is not to be expected with the infinite amount of overlying flux. This resembles the real situation for a small arcade of loops embedded in a large active region. With an estimated coronal magnetic Reynolds number of about 10^{12}, and with the numerical results giving no indication of strong current concentrations, indeed no significant reconnection can occur on a time-scale of up to 100 Alfven scale times (the duration of the simulation). Therefore, the conversion of magnetic energy into MHD wave energy may be the only efficient method that is available to shed excess free energy and, thus, for heating the corona. Details of this study are described by Marten, Sun and Wu (1992).

5 Two-Dimensional MHD Global Coronal Model: Steady State Streamers

In this subject, we have made some progress since we first constructed a streamer model (Steinolfson, Suess and Wu, 1982). Our motivation to revisit this problem was to extend the outer boundary farther away from the Sun (i.e. ~35 solar radii) and to gain the experience necessary for development of a three-dimensional model. Another motivation to develop such a model is the simulation of streamers in support of the Ultraviolet Coronagraph and Spectroheliograph (UVCS) and the Large Angle Spectrometric Coronagraph (LASCO) instruments on the Solar Heliospheric Observatory (SoHO). These instruments will be able to measure the temperature, density, and flow velocity vector in the corona. With model calculations, it will be possible, for example, to infer the magnetic vector. The results of the present study are presented by Wang *et al.* (1992a,b) and Noci *et al.* (1992). We shall briefly summarize some of the highlights in the following paragraph.

Figure 10 shows the steady state magnetic field lines for four cases: (a) Dipolar $\beta_o = 0.5$, (b) Quadrupole, $\beta = 0.5$, (c) Hexapole, $\beta = 0.5$, and (d) Dipole, $\beta = 0.2$. The relaxation times allowed to reach these equilibria are: (a) 22.22 hrs., (b) 16.7 hrs., (c) 18.06 hrs., and (d) 19.44 hrs. respectively, where β is evaluated at the equator of the solar surface. In each plot, four dashed lines are labelled "A, B, C, or D". These show the radial directions used for plotting the variables versus radius in each case. Thus, the $\beta = 0.5$ quadrupole plots will have variables versus radius at the pole (B), at the edge of the polar region (A), through the mid-latitude streamer (D), and in the equatorial open region (C). The dashed lines are along the direction of the grid. Since there is no grid point either exactly on the equator or exactly at the pole, these lines are slightly offset from those positions. The plasma parameters, radial velocity and total magnetic field strength, are presented in a pre-print (Wang, Wu, Suess and Poletto, 1992b) which is included in the Appendix.

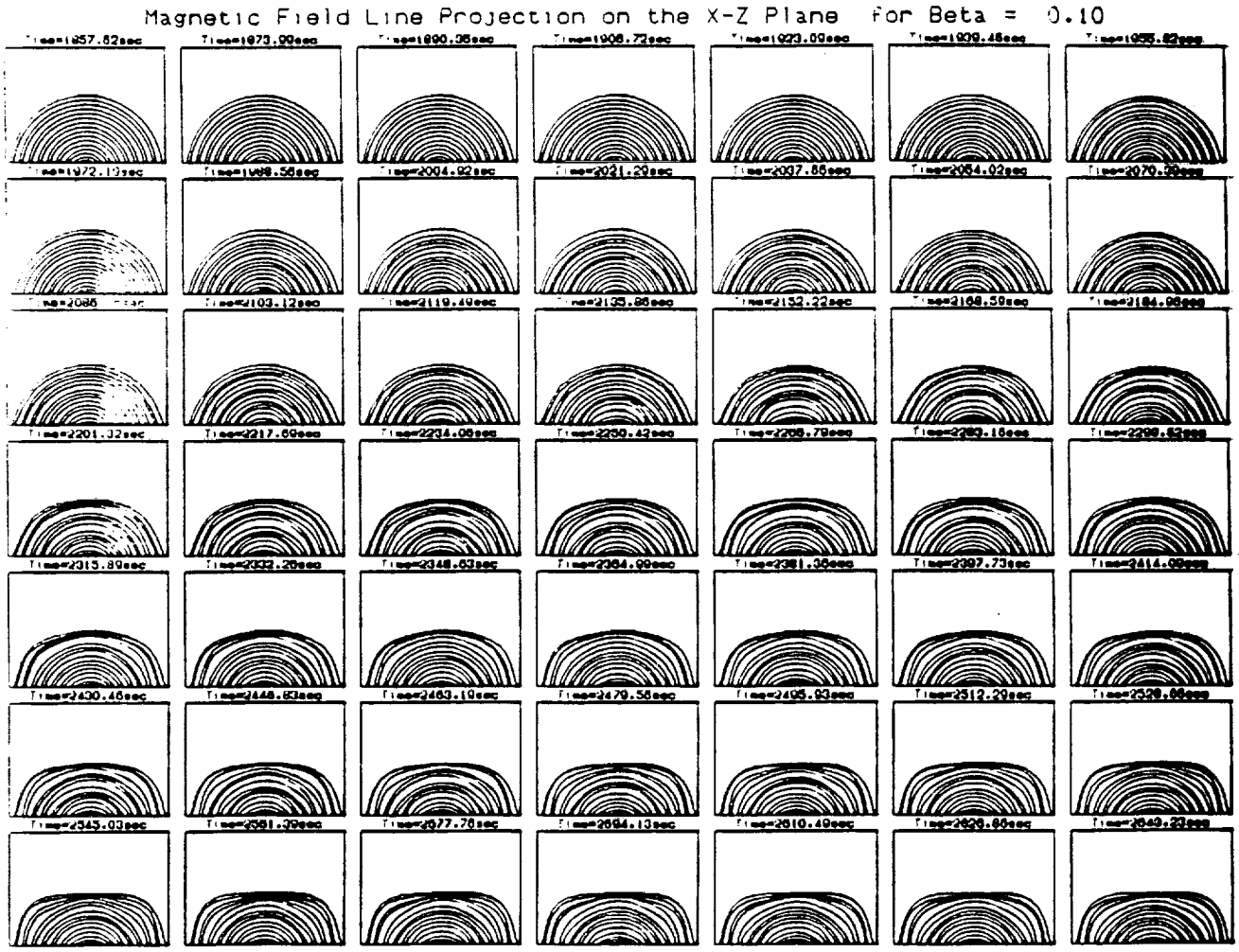

Figure 9: Numerical simulation of the evolution of the magnetic field in projection on the $x - z$ plane, which is perpendicular to the $x - y$ photospheric plane.

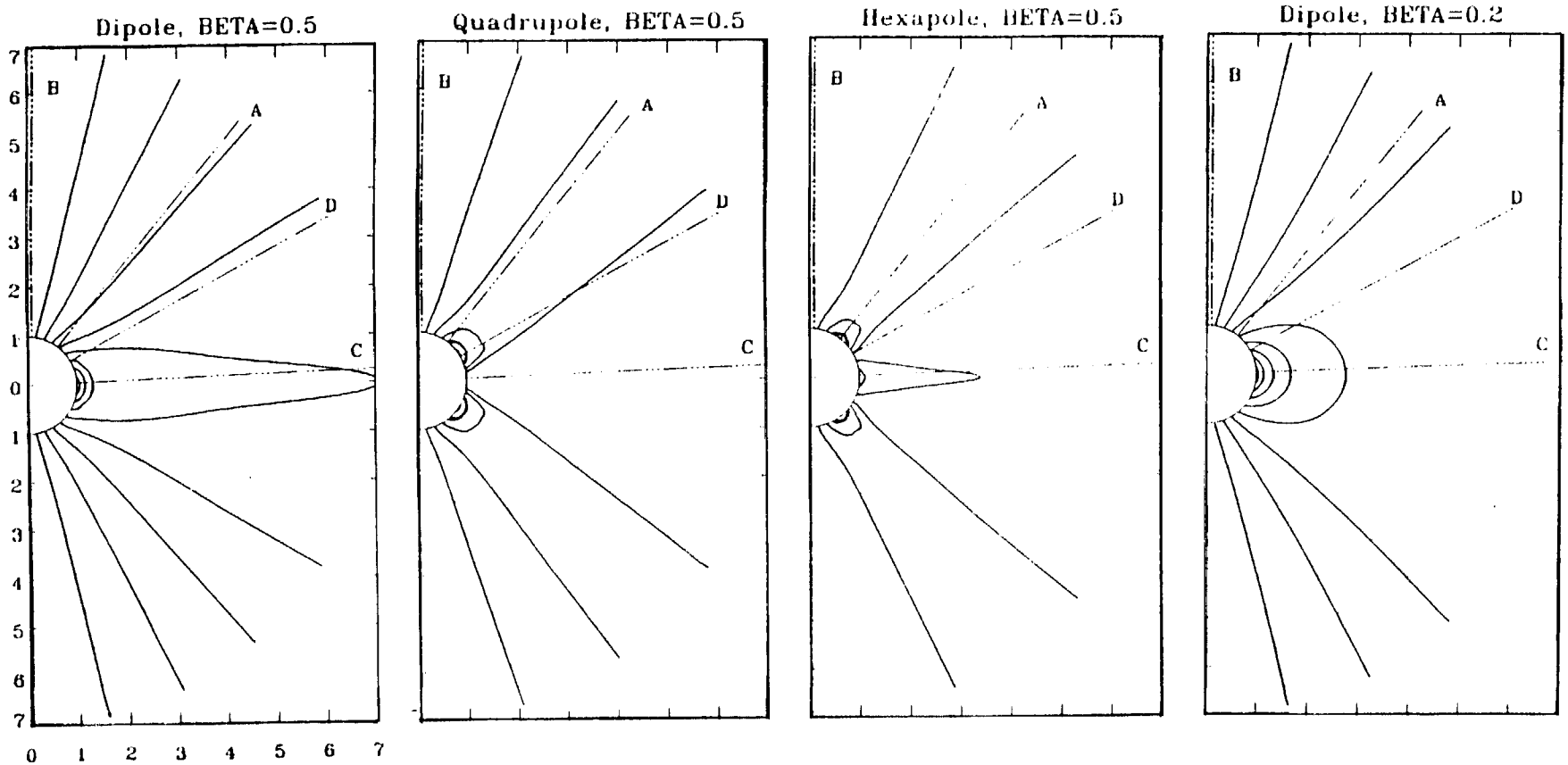

Figure 10. Steady state magnetic field line plots for the four cases: (a) Dipole, $\beta = 0.5$, (b) Quadrupole, $\beta = 0.5$, (c) Hexapole, $\beta = 0.5$, and (d) Dipole, $\beta = 0.2$. The relaxation times allowed to reach these equilibria are: (a) 22.22 hours, (b) 16.67 hours, (c) 18.06 hours, (d) 19.44 hours, respectively. In each plot, four dashed lines are labelled 'A,B,C, or D'. These show the radial directions used for plotting the variables versus radius in each case. Thus, the $\beta = 0.5$ quadrupole plots will have variables plotted versus radius at the pole (B), at the edge of the polar open region (A), through the mid-latitude streamer (D), and in the equatorial open region (C). The dashed lines are along the directions of the grid. Since there is no grid point either exactly on the equator or exactly at the pole, these lines are slightly offset from those positions.

6 REFERENCES

1. Harrison, R. A., and D. G. Sime, 1989, J. Geophys. Res., **94**, 2333.
2. Hundhausen, A. J., 1988, in Proc. Sixth International Solar Wind Conference (V. J. Pizzo, T. E. Holzer and D. G. Sime, Eds.) NCAR Tech. Note NCAR/NT-306+PROC., 181.
3. Kahler, S., 1987, Rev. Geophys. **25** 663.
4. Low, B. C. and Y. Q. Lou, 1990, Astrophys. J., **352**, 343.
5. Martens, P., M. T. Sun and S. T. Wu, 1992 in IAU Colloquium 133,, Eruptive Solar Flares (Z. Svestka, B. V. Jackson, and M. E. Machado, eds.) Springer-Verlag, Berlin.
6. Parker, E. N., 1972, Astrophys. J., **174**, 499.
7. Parker, E. N., 1987, Astrophys. J., **318**, 876.
8. Schmidt, H. V., 1964, Physics of Solar Flares (NASA SP-50), p. 107.
9. Steinolfson, R. S., S. T. Suess and S. T. Wu, 1982, Astrophys. J., **255**, 730.
10. Sudan, R. J., 1991, Proc. OSL Workshop, Capri.
11. Sun, M. T. and S. T. Wu, and Dryer 1992, **J. Comp. Phys.** (submitted).
12. Wang, Ai-Hua, S. T. Wu, S. T. Suess and G. Poletto, 1992a, in Proc. of the 3rd COSPAR Colloquium, Solar Wind VIII (E. Marsch and R. Schwenn, eds) Pergamon Press, Oxford, p. 311.
13. Wang, Ai-Hua, S. T. Wu, and S. T. Suess and G. Poletto, 1992b, **Solar Phys.** (submitted)
14. Webb, D. F. and B. V. Jackson, 1990, J. Geophys. Res., **95**, 20641.
15. Wu, S. T., M. T. Sun, H. M. Chang, M. J. Hagyard and G. A. Gary, 1990, Astrophys. J., **362**, 698.
16. Wu, S. T., M. T. Song, P. C. H. Martens and M. Dryer, 1991a, Solar Phys., **134**, 353.
17. Wu, S. T., M. T. Song and M. Dryer, 1991b, AIAA paper 91-1470.
18. Wu, S. T., C. L. Yin and W.-H. Yang, 1992, **Solar Phys. 142**, 313.
19. Wu, S. T. and F. S. Weng, 1992, **J. Atmospheric and Terrestrial Phys.**, **55**, 939.

Appendix

A TWO-DIMENSIONAL MHD GLOBAL CORONAL MODEL: STEADY-STATE STREAMERS

A.-H. WANG, S. T. WU
Center for Space Plasma and Aeronomic Research and Department of Mechanical Engineering, The University of Alabama in Huntsville, Huntsville, AL 35899, U.S.A.

S. T. SUESS
Space Science Lab, ES52, NASA Marshall Space Flight Center, Huntsville, AL 35812, U.S.A.

and

G. POLETTO
Osservatorio Astrofisico di Arcetri, 50125 Firenze, Italy

(Received 4 August, 1992; in revised form 22 February, 1993)

Abstract. We describe a two-dimensional time-dependent, numerical, magnetohydrodynamic model for the determination of the physical properties of coronal streamers fro the top of the transition zone ($R_\odot = 1$) to 15 $R_\odot$. Four examples are given: for dipole, quadrupole, and hexapole initial field topologies. The computed parameters are density, temperature, velocity, and magnetic field. In addition to the properties of the solutions, their accuracy is discussed. We use the model as the basis for a general discussion of the way boundary conditions are specified in this and similar simulations.

1. Introduction

We present results from a recently-developed numerical model of coronal structure. The immediate reasons for a new model were to extend the outer boundary farther from the Sun and to gain the experience necessary for development of a three-dimensional model. A result of this process has been a close examination of the physical details of the solution and how they depend on the way the boundary conditions are specified. An immediate application will be the simulation of streamers in support of the Ultraviolet Coronagraph and Spectroheliograph (UVCS) and the Large Angle Spectrometric Coronagraph (LASCO) on the Solar Heliospheric Observatory (SoHO). These instruments will be able to measure the temperature, density, and flow vector in the corona. With model calculations, it will be possible, for example, to estimate the magnetic field vector.

Numerical models of coronal structure have been published sporadically, at long intervals, over the past twenty years. The first (Pneuman and Kopp, 1971) demonstrated the feasibility of such models, treating isothermal flow and arriving at the solution by iterating on the electrical currents. However, a more efficient and flexible method is to consider an initial-boundary value problem in which the steady state is found holding the boundary conditions constant and allowing the solution to relax in time from an essentially arbitrary initial state. Steinolfson, Suess, and Wu (1982) applied this later technique to the analysis of a polytropic dipole configuration for a range of plasma β (ratio of internal pressure to mag-

Solar Physics **000**: 1–17, 1993.

GR 201018146 Grafikon: PIPS No. 32919
solah362.tex - Date: March 10, 1993 Time: 9:06

netic pressure). Steinolfson (1989, 1991) and Guo *et al.* (1992) have used this steady-state solution as the basis for studying coronal mass ejections and streamer evolution with shear, which can be simulated using a nearly identical numerical model. Details of the numerical schemes and results can be found in the referenced publications.

We revisited this problem for the reasons mentioned above. However, we also consider that such complex numerical models are rarely without problems or uncertainties. When the models are used for analysis of data and for predictions, the only reliable validation is to develop an independent model and compare the results. Even when both (or all) models are fundamentally correct, this process generally leads to new or deeper understanding of the problem. In the present case, this is precisely what has happened. We have gained a better insight into the physical basis of the criteria which should be adopted in specifying boundary conditions. The results from this constitute an important part of the present study.

The physical and numerical simulation is described in Section 2. Section 3 details numerical models of dipole, quadrupole, and hexapole magnetic fields. Section 4 is a discussion of numerical precision of the solution and the boundary conditions, putting the discussion into context with earlier models so far as is possible. Section 5 contains our summary and conclusions.

2. The Physical and Numerical Simulation

We assume axisymmetric, single fluid, polytropic, time-dependent ideal magnetohydrodynamic flow and perform the calculation in a meridional plane defined by the rotational symmetry axis of the magnetic field. The coordinates are (r, θ, ϕ) with ϕ being the ignorable coordinate. For the magnetic field boundary condition, we take the radial field component at the lower boundary to be that given by a vacuum dipole, quadrupole, or hexapole potential magnetic field. The flow therefore has reflective symmetry across the equator and the calculation need be done in only one quadrant. The equations of motion that describe this flow are:

$$\frac{\partial \rho}{\partial t} + \frac{\partial}{\partial r}(\rho v_r) = \left(\frac{\rho v_\theta}{r}\right) = -\frac{2\rho v_r}{r} - \frac{\rho v_\theta}{r}\cot\theta\,. \tag{1a}$$

$$\frac{\partial v_r}{\partial t} + v_r\frac{\partial v_r}{\partial r} + \frac{B_\theta}{\mu\rho}\frac{\partial B_\theta}{\partial r} = \frac{1}{\rho}\frac{\partial p}{\partial r} = \frac{v_\theta}{r} + \frac{\partial v_r}{\partial \theta} - \frac{B_\theta}{\mu\rho r}\frac{\partial B_r}{\partial \theta} =$$

$$= -\frac{GM_\odot}{r^2} + \frac{v_\theta^2}{r} - \frac{B_\theta^2}{\mu\rho r}\,. \tag{1b}$$

$$\frac{\partial v_\theta}{\partial t} + v_r\frac{\partial v_\theta}{\partial r} - \frac{B_r}{\mu\rho}\frac{\partial B_r}{\partial r} = \frac{v_\theta}{\partial \theta} + \frac{B_r}{\mu\rho r}\frac{\partial B_r}{\partial \theta} + \frac{1}{\rho r}\frac{\partial p}{\partial \theta} = \frac{B_r B_\theta}{\mu\rho r} - \frac{v_r v_\theta}{r}\,, \tag{1c}$$

$$\frac{\partial B_r}{\partial t} - \frac{\partial}{\partial \theta}\left(\frac{v_r B_\theta - v_\theta B_r}{r}\right) = \frac{1}{r}(v_r B_\theta - v_\theta B_r)\cot\theta\,. \tag{1d}$$

$$\frac{\partial B_\theta}{\partial t} + \frac{\partial}{\partial r}(v_r B_\theta - v_\theta B_r) = -\frac{1}{r}(v_r B_\theta - v_\theta B_r), \tag{1e}$$

$$\frac{\partial p}{\partial t} + \gamma p \frac{\partial v_r}{\partial r} + v_r \frac{\partial p}{\partial r} + \frac{\gamma p}{r}\frac{\partial v_\theta}{\partial \theta} = \frac{\gamma p}{r}(2v_r + v_\theta \cot\theta). \tag{1f}$$

The dependent variables are the density, ρ, the pressure, p, the radial and meridional velocities, v_r and v_θ, and the radial and meridional magnetic fields, B_r and B_θ. The constants $M_\odot$, G, γ, and μ are the solar mass, gravitational constant, the polytropic index and the magnetic permeability.

These equations are solved in a computational domain extending from the Sun (1 $R_\odot$) to 15 $R_\odot$, from the pole to the equator. It is assumed that meridional flow is zero at the pole and equator. The grid is divided so that there are 37 gridpoints in the radial direction and 22 gridpoints in the meridional direction, with the radial grid size slowly increasing with radius. The meridional grid is divided so that points lie equi-distant on either side of $\theta = 0$ and $\theta = 90°$, at $\theta = -2.25°$, 2.25°, 6.75°, ..., 87.75°, 92.25°. The algorithm adopted here is the Full-Implicit Continuous Eulerian (FICE) scheme described by Hu and Wu (1984). For time stepping a second-order accurate toward differencing scheme is used, with the step size being of the same order as given by the Courant condition because the magnetic field is calculated explicitly. Smoothing is used when gradients become too large, i.e., at shocks (which do not occur here). At the inner boundary, the flow is subsonic and sub-Alfvénic so that two of the six independent variables are calculated using compatibility relations (Hu and Wu, 1984). A brief summary of the compatibility conditions for the present model is given in the Appendix, along with details on how the boundary values and conditions are applied. We choose to specify the radial and meridional magnetic fields, temperature, and density. The radial and meridional flow speeds are computed from compatibility relations (i.e., Equations (A.1) and (A.2)). At the outer boundary, the flow is restricted to being both supersonic and super-Alfvénic. In this case, all variables at that boundary can be calculated by simple linear extrapolation from the first (or first two) grid points inside the boundary. In this study, we did not perform the comparison between the present boundary conditions and conventional boundary conditions. However, in a recent study by Sun (1991), it was shown that the statement of the boundary conditions in the Appendix eliminates the spurious waves generated by boundary disturbances and which can cause numerical instability.

We start with an essentially initial state and allow the flow to relax in time while holding the boundary values constant. In the present case the initial flow field is a polytropic, hydrodynamic solution to the steady-state radial flow equation of motion (e.g., Parker, 1963) superimposed on a potential magnetic field. That this is neither a self-consistent nor stable solution to the steady-state MHD equations is irrelevant since the flow is allowed to evolve in time under the control of the equations of motion. The main concerns are that the numerical solution be stable and of sufficient accuracy to define the physically interesting aspects of the solution, and that the relaxation proceed long enough that an acceptably close

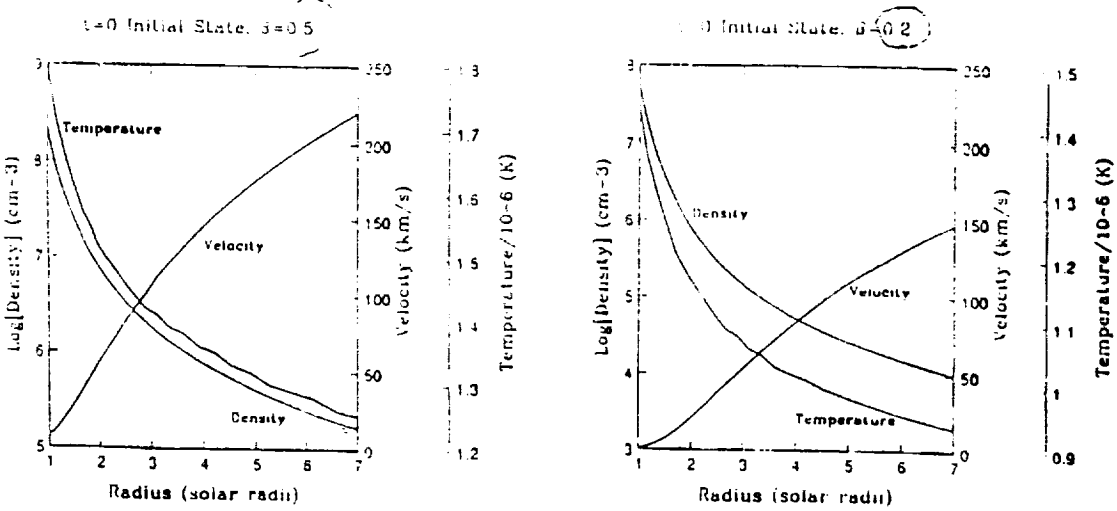

Fig. 1. Density, temperature, and velocity profiles in radius that were used for the initial ($t = 0$) state in the relaxation. On the left are the profiles for the $\beta = 0.5$ cases and on the right are the profiles for the $\beta = 0.2$ case. Note that, except for the velocity scales, the scales differ between the two panels. Because the polytropic index is near unity, temperature changes slowly with radius and the irregularities in the temperature profiles should be interpreted as noise.

approximation to the steady state has been reached. We address these issues briefly in Section 4.

3. Detailed Results from Four Specific Models

We report here on four specific models. The results are grouped first according to the way in which the physical variables are plotted (i.e., either versus radius or versus polar angle) and second according to which of the four examples the plot is for. In these four examples, three magnetic field geometries are used: a dipole, a quadrupole, and a hexapole; the scalar potentials are therefore proportional to $P_2(\cos\theta)$, $P_3(\cos\theta)$, and $P_4(\cos\theta)$, respectively, where $P_n(\cos\theta)$ is the Legendre polynomial of degree n. There are two dimensionless free parameters: the polytropic index, γ, and the plasma, β. We use $\gamma = 1.05$ in all cases, $\beta = 0.5$ for all three field geometries, and, in addition, do a dipole calculation for $\beta = 0.2$. In these case, β is evaluated at 1.0 $R_\odot$ at the equator, where the field strength is 1.67 G both for $\beta = 0.5$ and $\beta = 0.2$. For the high β cases, the base temperature and density are 1.8×10^6 K and 2.25×10^8 cm^{-3}. For the low β case, they are 1.44×10^6 K and 5.61×10^7 cm^{-3}. The three magnetic field geometries naturally lead to a single equatorial streamer, a mid-latitude streamer, and both an equatorial and a mid-latitude streamer for the dipole quadrupole and hexapole, respectively.

Results from the four examples will be referred to as follows:

(a) Dipole, $\beta = 0.5$;

(b) Quadrupole, $\beta = 0.5$;

(c) Hexapole, $\beta = 0.\overline{5}$.

(d) Dipole, $\beta = 0.2$.

The initial state temperature, density, and velocity profiles are shown in Figure 1. The temperature curves appear irregular due to the small change in temperature over the relatively large radial range – a consequence of the polytropic index being near unity. Only three significant figures were retained after the calculation so what is seen here is roundoff error in the plotted results rather than in the computed results.

The final, steady-state magnetic field geometries for the four cases are shown in Figure 2. Here is seen the well-known property that the flow is nearly radial beyond 3–4 $R_\odot$. The flow is field-aligned everywhere and field lines which cross the outer boundary reach to ∞. The streamers are those volumes which are magnetically closed (i.e., the field lines return to the surface of the Sun) and it is evident that relatively small volumes in the streamers remain magnetically closed in comparison to the initial state where all field lines were closed. These closed volumes are surrounded by a low density shell but, as will be shown below, the densities in the large coronal hole-like open regions are otherwise only slightly lower than in the streamers. In each panel of Figure 2, four dashed lines are shown and labelled A, B, C, or D. These lines indicate the radial directions used below to plot variables versus radius.

The physical times allowed for the relaxation in these four examples were: (a) 22.22 hours for the $\beta = 0.\overline{5}$ dipole; (b) 16.67 hours for the $\beta = 0.5$ quadrupole; (c) 18.06 hours for the $\beta = 0.\overline{5}$ hexapole; (d) 19.44 hours for the $\beta = 0.2$ dipole. These times are determined by how long it takes for any fluctuation to be advected out through the outer boundary of the solution domain. This in turn depends on how large the flow speed is and whether the fluctuations represent inward propagating waves. In general, the times listed above are the minimum required for a stationary fluctuation (i.e., non-propagating in the solar wind frame) to be advected from 1 $R_\odot$ to 15 $R_\odot$ at a typical flow speed in the open regions. This sometimes leads to small residuals in the relaxation near the outer boundary at 15 $R_\odot$, but the solutions inside 7 $R_\odot$ that are shown here are quite steady. This is another point that will be reviewed in Section 4.

Figures 3 and 4 are plots of density and radial velocity versus radius. The plots are made in the directions indicated in Figure 2 so that, for example, in each panel of Figure 3 the density is plotted in the four directions A, B, C, and D indicated in the corresponding panel of Figure 2. In both of Figures 3 and 4, the four panels corresponding to the four panels in Figure 2 are clearly labeled. The density profiles have been divided by their corresponding initial state ($t = 0$) profiles from Figure 1 because the density changes by several orders of magnitude between the Sun and 15 $R_\odot$. The plots here extend only to 7 $R_\odot$ because there is no new information contained outside this radius – the flow is already supersonic and essentially radial.

Turning briefly to each figure individually, we begin by noting that a density enhancement is indicated by values grater than unity, and *vice versa*. The density

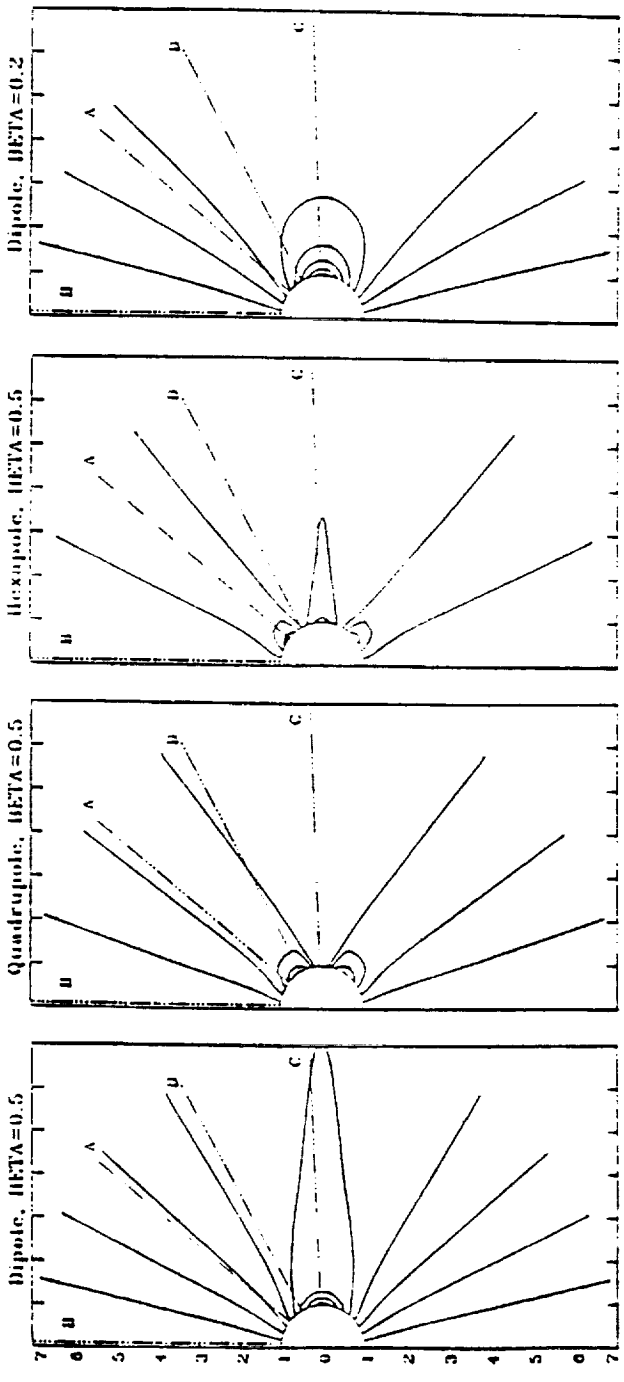

Fig. 1. Steady state magnetic field line plots for the four cases: (a) Dipole, $\beta = (0.5)$ (b) quadrupole, $\beta = (0.5)$ (c) hexapole, $\beta = (0.5)$ and (d) dipole, $\beta = 0.2$. The relaxation times allowed to reach these equilibria are: (a) 22.22 hours, (b) 16.67 hours, (c) 18.06 hours, (d) 19.44 hours, respectively. In each plot, four dashed lines are labelled 'A, B, C, or D'. These show the radial directions used for plotting the variables versus radius in each case. Thus, the $\beta = 0.5$ quadrupole plots will have variables plotted versus radius at the pole (B), at the edge of the polar open region (A), through the mid-latitude streamer (D), and in the equatorial open region (C). The dashed lines are along the directions of the grid. Since there is no grid point either exactly on the equator or exactly at the pole, these lines are slightly offset from those positions.

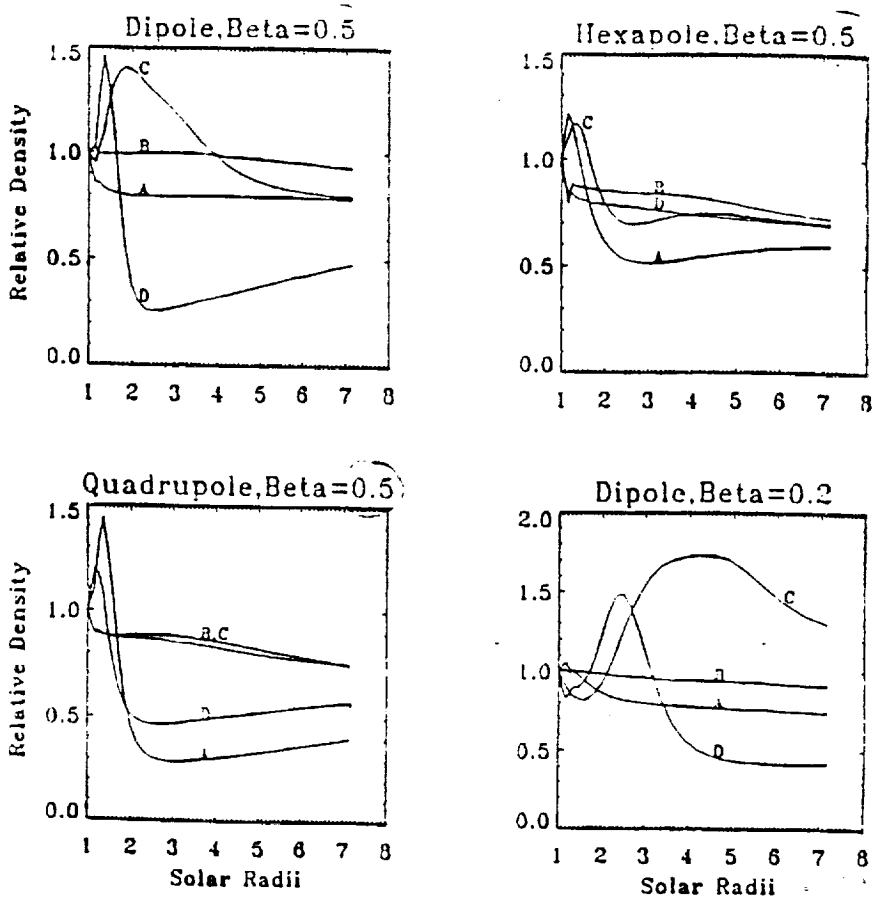

Fig. 3. Density as a function oradius. Each panel is for the corresponding case in Figure 2, as labelled. The curves are plotted along the directions shown in Figure 2. For example, the four curves for the $\beta = 0.5$ hexapole labelled (A, B, C, D), are along the four directions shown in the third panel of Figure 2 and labelled in the same manner. Each curve has been divided by the initial profile (see Figure 1). A density enhancement is indicated by values greater than unity, and *vice versa*. The density concentrations in the streamers are clearly visible, generally being on the order of 25% to 50% above the initial state.

concentrations in the streamers here are clearly visible, generally being on the order of 25% to 50% above the initial state. The base density for the $\beta = 0.5$ cases is close to that reported by Allen (1955) for the base of the quiet corona and the density profile shown here has generally the right behavior for streamers – as shown by curves C for cases (a), (c), and (d), and curve D in case (b). Curve D for case (a), the $\beta = 0.5$ dipole, is an example of the density deficit on the flank of a streamer that is typical of the results for all the examples. In contrast, the density in the centers of the open regions (curve B in all cases, curve C in case (b), and curve D in case (c)) is little different from the initial state, being only slightly smaller. This is only surprising when comparison is made to coronal hole observations (Munro

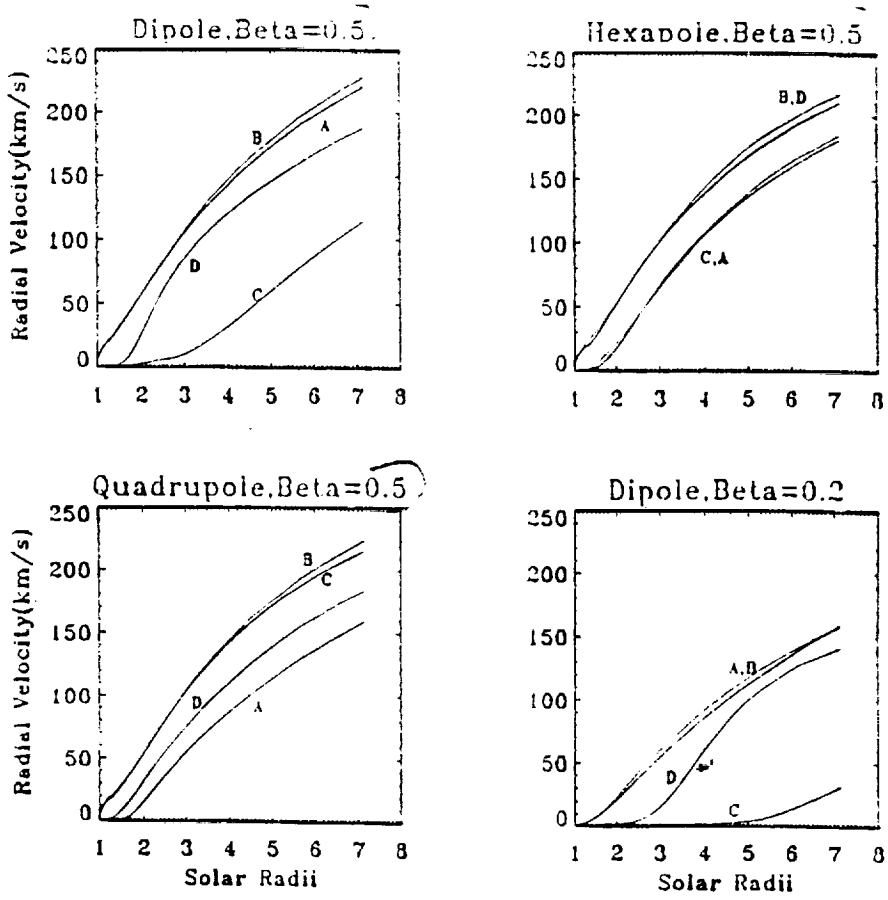

Fig. 4. Radial velocity as a function of radius. Each panel is for the corresponding case in Figure 2. The curves are plotted along the directions shown in Figure 2, as in Figure 3. The velocity inside the streamers is seen to be essentially zero.

and Jackson, 1977) wherein the density was reported to be more than an order of magnitude less than in streamers. This difference is a natural consequence of the properties of a polytropic model and the choice we have made for the boundary conditions on temperature and density – that they be independent of polar angle. The choice leads to both the high density shown here and the low flow speeds shown below on open field lines, irrespective of the open streamline geometry. To model true coronal hole flow with a polytropic gas would require at least an elevated temperature in the open regions and probably also a lower density at the base (Suess *et al.*, 1977; Suess, 1979).

The radial velocity is shown in Figure 4, at the positions indicated in Figure 2. As described above, and as is generally the case in polytropic models, the flow speed in the open regions is similar to the undisturbed initial flow speed shown in Figure 1. In the streamer, the flow speed is essentially zero and it is reduced

on the adjacent open field lines due, apparently, to the strongly inclined flow direction more than to geometry. The nonzero outflow above streamers (e.g., at $R = 7.14\ R_\odot$, at the equator of the $\beta = 0.5$ dipole) refers to the open field region above the streamer's cusp. The $\beta = 0.2$ dipole is the most extreme example of this – and the flow speed is nearly identical to the initial speed everywhere except on closed field lines, directly above the center of the streamer, and on the highly inclined field lines immediately adjacent to the streamer – where the difference is still rather small.

We do not plot the temperature since, due to the polytropic index being 1.05, it varies by only a few percent throughout the computation domain. However, this is an 'effective temperature' because a polytropic energy equation with a polytropic index of 1.05 is equivalent to a large amount of energy being added to the flow. Nowhere is the form of this energy specified, nor what the conversion and dissipation mechanisms are. However, it has been shown that a polytropic index on the order 1.05 is required to reproduce observations of coronal densities (Suess *et al.*, 1977).

Finally, the magnetically open regions, although equivalent to coronal hole flows, do not simulate coronal holes because the flow speeds are far too small. To obtain reasonable flow speeds in this model it would be necessary to have the temperature vary across the base of the open region – which is well within the capability of the model. Such a variation has been shown to reproduce all the known properties of coronal hole flow and lead to accurate simulations of the geometry, with the effective temperature being larger in the center of the hole than at the edge (Suess *et al.*, 1977). In contrast to the open regions, the densities in the closed regions are similar to observed streamer densities and we feel this model is therefore a good approximation to streamer geometry. The temperature must still be qualified as an effective temperature, but can be used for diagnostic purposes in combination with planned observations on SoHO/UVCS.

Some of the results can be better viewed and more easily understood when plotted versus polar angle at different heliocentric distances, than versus radius at constant polar angles. Such plots are shown for the density, radial velocity, and total field strength in Figures 5, 6, and 7, respectively.

Figure 5 shows the density drop adjacent the streamer. In the panel for the $\beta = 0.5$ dipole, this drop is quite large, well resolved, and leads into the density enhancement inside the equatorial streamer. The only place this does not occur is at the base – where the density is held constant. The width of the density enhancement in the streamer decreases with height, just as the width of the streamer itself decreases with height (e.g., Figure 2). Essentially the same thin is seen for the $\beta = 0.2$ dipole wiht the following quantitative differences: (i) The streamer is much higher and wider. (ii) The density depletion on the flanks has a smaller amplitude. These differences are the primary reason we conclude that solar streamers are better described by a $\beta = 0.5$ plasma than by a $\beta = 0.2$ plasma. Qualitatively, a similar result is found for the quadrupole and hexapole. However, it is obvious that the

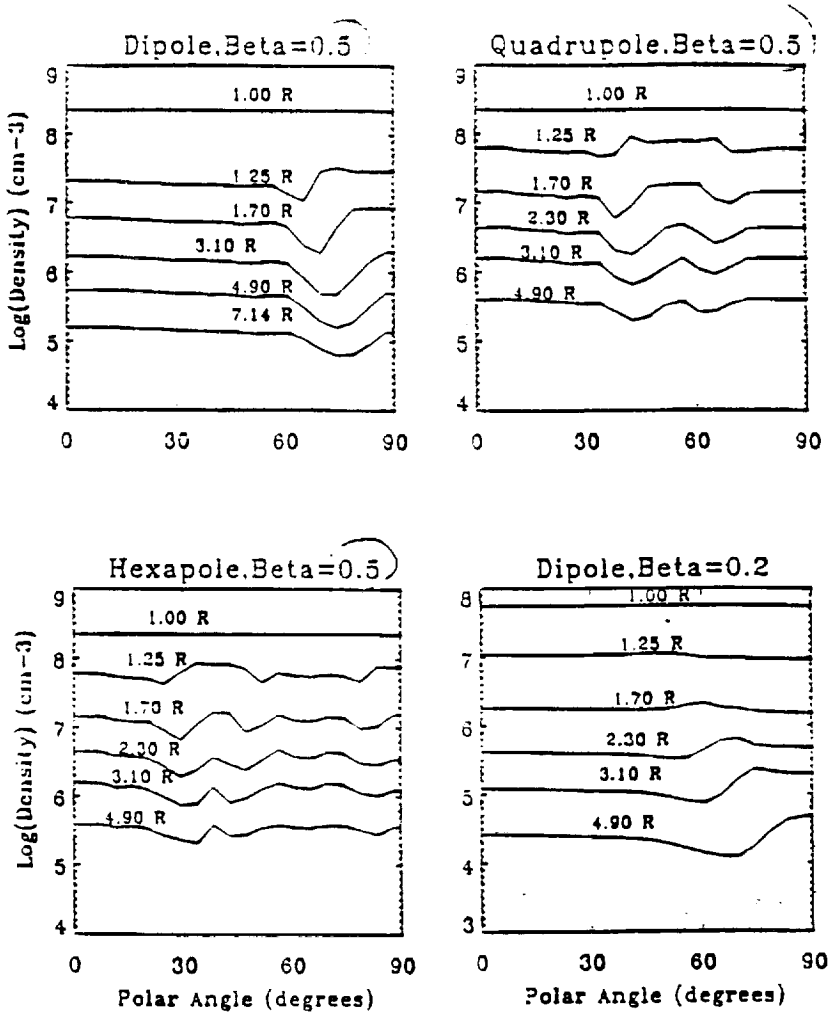

Fig. 5. Density versus polar angle, between the pole (0°) and the equator (90°). Each of the curves is labelled according to the heliocentric distance it refers to. Thus the curves labelled 1.70 R indicate the density at 1.70 $R_\odot$ heliocentric radius. The density at the base is constant and so the curves there are flat. Above the base, there is a small density enhancement in the streamer (ca. 5% to 50%) and a trough in density at the edge of the streamer. In the middle of the open region, the density is very close to what it was in the initial state (see also Figure 3). The reason it is not small is that we have used constant temperature and density at the base. To produce a true coronal hole-like profile would have required at least an increase in the temperature at the base of the open region (Suess *et al.*, 1977).

hexapole is only marginally resolved with the present grid density – there is really only one meridional grid point inside the mid-latitude streamer at any given height.

The radial velocity in Figure 6 drops precipitously from the magnetically open region to the inside of the streamer. That the velocity is not identically zero inside the streamer is a result of numerical diffusin and is a measure of this numerical

artifact in the FICE scheme. For example, at 1.70 $R_\odot$ in the $\beta = 0.5$ dipole, the velocity drops from ca. 60 km s^{-1} is hardly above the noise level in the plots and the associated kinetic energy is too small to affect the dynamics of the solution. Such 'slippage' will, nevertheless, occur in all numerical solutions. At larger heights (e.g., 4.90 and 7.14 $R_\odot$) there is small, but finite flow near and in the neutral sheet dividing regions of opposite magnetic polarity. This is qualitatively like what is observed in the solar wind in the interplanetary medium. The $\beta = 0.2$ dipole again exhibits properties unlike the Sun in the sense that the very low flow speeds inside the streamer seem to still exist even at 7.14 $R_\odot$ – far outside the observed extent of closed streamers.

Figure 7 shows the variation of the total magnetic field strength, $(B_r^2 + B_\theta^2)^{1/2}$, across the streamers. The most interesting thing to note in these plots is the enhancement in total field strength on the flanks of the streamers. This is what 'confines' the streamers. The field strength for the $\beta = 0.2$ dipole is seen to vary smoothly, with little distinct evidence of the streamer. This is just another indication that the presence of the plasma has had little effect on the field geometry in this low-β case.

4. Accuracy and Stability of Calculations

This numerical model has been found to be weakly subject to the Courant condition on size of time step. Therefore, the size of the time step decreases as the largest values of the temperature and magnetic field increase – along with the maximum sound and Alfvén speeds anywhere in the grid. Counteracting this, the higher characteristic speeds lead to a somewhat faster relaxation time. However, generally shorter time steps are required for smaller β calculations. The flow speed also plays an important role in determining the relaxation time to a steady state – the initial state is a disequilibrium configuration. This imbalance must have time to be advected from the base through the outer boundary. The physical time this takes can be estimated by taking a typical (but small) value for the flow speed and caculating how long it would take the plasma to flow at this speed from the base to the outer boundary. For example, at 150 km s^{-1}, to 15 $R_\odot$, this takes 18 hours (relaxation times we have used here are given in Figure 1).

A second consideration is gridpoint resolution. The grid used in these examples is 4.5° in latitude and about 0.24 $R_\odot$ in radius near the base – increasing slowly with radius. This is sufficient to adequately resolve the geometry and flow on the scale shown in Figure 2. However, if finer scale information is required in, for example, the core of the streamers, a denser grid would be required.

Always a serious consideration in these time-dependent, non-Cartesian MHD calculations is the conservation of magnetic flux – that $\nabla \cdot \mathbf{B} = 0$ is maintained at all times. The condition is maintained here through accurate differencing rather than a self-correcting scheme. No anomalous acceleration due to errors in flux conservation is apparent in the results. The numerical scheme is pressure-based so it is limited by stability to large and moderate β values (e.g., $\beta \geq 0.1$) – which

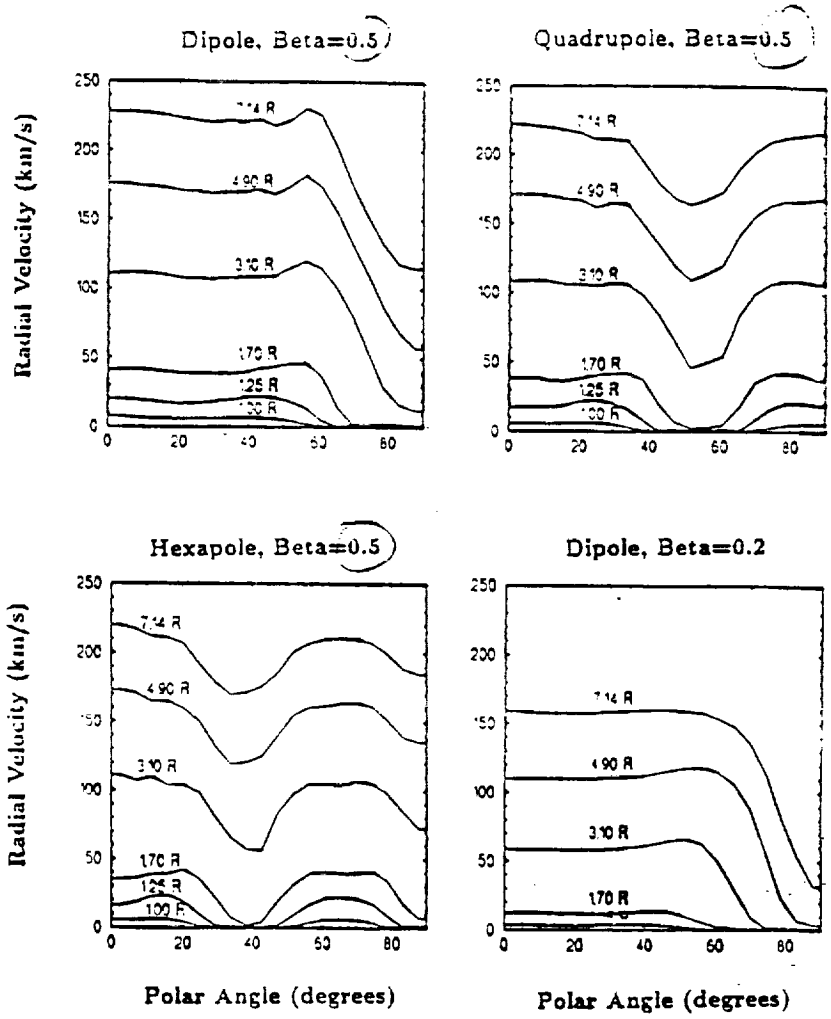

Fig. 6. Radial velocity versus polar angle, between the pole and the equator. Each curve, plotted for different heliocentric distance, is labelled in the same manner as in Figure 5. The velocity in the magnetically closed regions is essentially zero. The reason it is not identically zero is that there is a small amount of numerical diffusion – quite small as indicated by the velocity being less than 10 km s^{-1} inside the $\beta = 0.5$ dipole streamer at 2.30 $R_\odot$.

turns out to be the same restriction for maintaining $\nabla \cdot \mathbf{B} = 0$ to the required degree.

Finally, the energy equation

$$\left(\frac{\partial}{\partial t} + \mathbf{v} \cdot \nabla\right)\left(\frac{p}{\rho^\gamma}\right) = 0$$

reduces to $\mathbf{v} \cdot \nabla(p/\rho^\gamma) = 0$ when a steady state is reached, which means that (p/ρ^γ) is then a streamline constant. This becomes an analytic test of the achievement of a

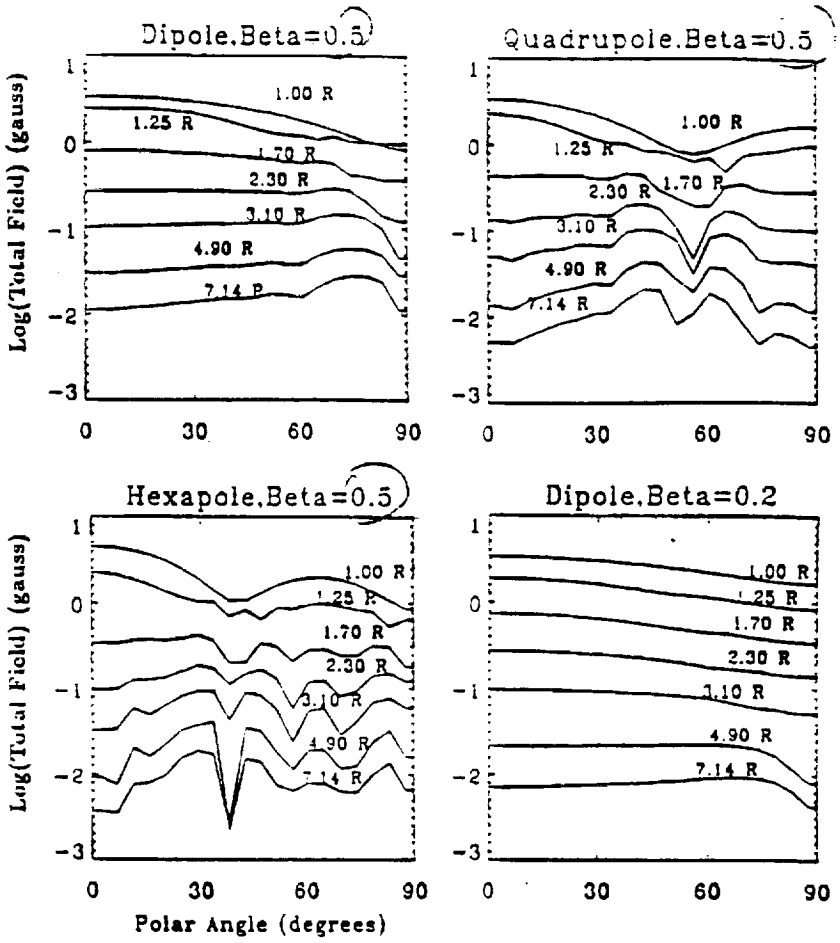

Fig. 7. The total magnetic field ($(B_r^2 = B_\theta^2)^{1/2}$) versus polar angle, between the pole and the equator. Each curve, plotted for different heliocentric distance, is labelled in the same manner as in Figure 5. The field in the vicinity of the current sheet above the cusp in the streamers has a greatly reduced amplitude, as would be expected. The effect is amplified above the mid-latitude streamers.

steady-state solution in our case. The boundary values of p and ρ are the same at all latitudes. Therefore, $(p/\rho^\gamma) = 0$ has the same value everywhere in the computation regime as it has on the boundary if a steady state has been reached. We have checked this for the cases shown in Figure 2 and find that for the dipole and quadrupole it is constant to within a maximum of 1% and for the hexapole it is constant to within a maximum of 4% (average values over the whole grid are less than 1% in all cases).

5. Discussion

The new feature of this model, with respect to analogous simulations, is the extension of the outer boundary to 15 $R_\odot$. This is not a conceptual advance, but this and

the stability and ruggedness of the code make it very useful for simulating realistic coronal conditions. We present new results for quadrupole and hexpole fields, with their accompanying mid-latitude streamers and open magnetic field regions. The Alfvén speed ranged between 800 km s^{-1} and a few tens of km s^{-1}. This is lower than is believed appropriate for the corona (Suess, 1988), but we expect our model will now enable simulations with higher Alfvén speeds.

When comparing our results to those of Steinolfson, Suess, and Wu (1982; henceforth referred to as SSW), an interesting, an dimportant difference becomes apparent. In the present calculation, we have held the density and temperature constant at the base, allowing the velocity (and, hence, the mass flux) to 'float' with time in accordance with the compatbility relations determining the velocity from the solution inside the computational domain. In contrast, SSW hold the temperature and velocity constant at the base and allow the density to change according to the compatibility relationships. SSW determine the location of the streamer by locating close field lines and allowing the velocity to decrease to zero at the feet of these field lines. A consequence is that inside the streamer, the final density is considerably higher than the initial density and this is the primary reason for the quantitative differences between their results and ours.

There is an important consequence of this difference in boundary conditions between SSW and the present calculation: the plasma β is computed using the temperature, density, and magnetic field at the equator and at 1 $R_\odot$. This is invariant in the present calculation, but in SSW this number is different in the final, steady state than at the beginning: there β was computed using the initial values. Therefore, in SSW in the steady-state solution is actually larger than stated for each example they did. Thus, our calculation for a dipole with $\beta = 0.2$ (case (d)) corresponds to cases for $\beta \leq 0.1$ in SWW. We feel that the way we have done the analysis more closely corresponds to what occurs and what is physically known for the Sun and therefore leads to a more precise definition of the problem. So, we conclude that the present study has demonstrated a preferable treatment of the boundary conditions in comparison to earlier calculations.

A consequence ~~of the~~ precise examples we have one in cases (a) through (d), with constant temperature and density, is the flow speed an dhigh density in the magnetically open regions – in comparison to what is believed to be the case in solar coronal holes. This is a natural consequence of using a polytropic gas in which the flow speed is strongly dependent on base temperature. It also does not reflect suggestions from analysis of Skylab data that densities at the base of coronal holes may be a factor of two smaller than at the base of streamers (G. Noci, private communication). In a continuation of this study, we will produce models with varying temperature and density at the base. The variation in temperature will, because it is an 'effective temperature', reflect a difference in energy balance and distribution between the base of coronal holes and streamers instead of a true temperature difference.

Acknowledgements

AHW and STW are supported by NASA Grant NAGW-9. STS has been supported by a grant from the Cosmic and Heliospheric Physics of NASA. GP acknowledges support from ASI (Italian Space Agency) and the University of Alabama in Huntsville.

Appendix. The Inner Boundary Conditions According to the Projected Normal Characteristic Method; a 2D Case

The inner boundary conditions are obtained according to the method of projected characteristics (Nakagawa, Hu, and Wu, 1987) with the FICE algorithm (Hu and Wu, 1984). For the two-dimensional case, the Alfvénic mode does not exist, therefore, there are six eigenvalues. These six eigenvalues lead to six projected normal characteristics and to six compatibiliity equations (see Wang, 1992; for derivation). At the inner boundary, since $v_r \geq 0$ and $v_r < V_s$, V_f, the characteristics $dr/dt = v_r - V_s$ and $dr/dt = v_r - V_f$ are towards the lower boundary from interior (i.e., outgoing) and need to be considered. There are four incoming characteristics (v_r, $v_r + V_s$, $v_r + V_f$, and one that is degenerate because of the model symmetries), so four variables can be specified at the boundary. Two other variables need to be calculated from related compatibility equations. We choose the values of B_r, B_θ, ρ, and T to be specified, leaving two quantities (i.e., v_r and v_θ) to be computed according to following compatibility equations:

$$\frac{\partial v_r}{\partial t} = \frac{V_s B_- + V_f C_-}{\rho V_s V_f (V_s^2 - V_f^2)}, \tag{A.1}$$

$$\frac{\partial v_\theta}{\partial t} = \frac{V_s (v_A^2 - V_s^2) B_- - V_f (V_f^2 - V_A^2) C_-}{V_s V_f (V_f^2 - V_s^2) B_r B_\theta}, \tag{A.2}$$

with the corresponding variables simplified in two dimensions as follows:

$$v_A^2 = b_r^2 = \frac{B_r^2}{\rho}, \tag{A.3}$$

$$a^2 = \gamma RT, \tag{A.4}$$

$$b^2 = \frac{(B_r^2 + B_\theta^2)}{\rho}, \tag{A.5}$$

$$V_f^2 = \frac{1}{2} a^2 + b^2 + [(a^2 + b^2)^2 - 4a^2 b_r^2]^{1/2}, \tag{A.6}$$

$$V_s^2 = \frac{1}{2} a^2 + b^2 + [(a^2 + b^2)^2 - 4a^2 b_r^2]^{1/2}, \tag{A.7}$$

$$B_- = \rho (V_f^2 - V_A^2) V_f (v_r - V_f) \frac{\partial v_r}{\partial r} - B_r B_\theta V_f (v_r - V_f) \frac{\partial v_\theta}{\partial r} -$$

$$-(V_f^2 - V_A^2)(v_r - V_f)\frac{\partial p}{\partial r} - B_\theta V_f^2(v_r - V_f)\frac{\partial B_\theta}{\partial r} +$$

$$+\rho(V_f^2 - V_A^2)V_f V_\theta \frac{1}{r}\frac{\partial v_r}{\partial \theta} - \frac{B_\theta v_\theta V_f^2}{r}\frac{\partial B_\theta}{\partial \theta} -$$

$$-[\rho a^2(V_f^2 - V_A^2) + B_\phi^2) + B_r B_\theta V_f v_\theta]\frac{1}{r}\frac{\partial v_\theta}{\partial \theta} -$$

$$-\left[v_\theta(V_f^2 - V_A^2) + \frac{B_r B_\theta V_f}{\rho}\right]\frac{1}{r}\frac{\partial p}{\partial \theta} - \frac{B_\theta v_f^3}{r}\frac{\partial B_r}{\partial \theta} -$$

$$-\frac{v_r V_f^2}{r}[2\rho(V_f^2 - V_A^2) - B_\theta^2] - \frac{V_f^2 B_\theta v_\theta}{r}(B_r + B_\theta \operatorname{ctg}\theta) -$$

$$-\frac{v_\theta V_f^2}{r}[\rho(V_f^2 - V_A^2) - B_\theta^2]\operatorname{ctg}\theta - \frac{v_r v_\theta B_\theta B_r V_f}{r} -$$

$$-\frac{\rho V_f V_\theta^2}{r}(V_f^2 - V_A^2) + \frac{V_f^3 B_\theta^2}{r} + \rho g(V_f^2 - V_A^2)V_f \,. \tag{A.8}$$

$$C_- = \rho(V_A^2 - V_s^2)V_s(v_r - V_s)\frac{\partial v_r}{\partial r} - B_r B_\theta V_f(v_r - V_s)\frac{\partial v_\theta}{\partial r} -$$

$$-(V_A^2 - V_s^2)(v_r - V_s)\frac{\partial p}{\partial r} + B_\theta V_s^2(v_r - V_s)\frac{\partial B_\theta}{\partial r} -$$

$$+\rho(V_A^2 - V_s^2)V_s V_\theta \frac{1}{r}\frac{\partial v_r}{\partial \theta} - \frac{B_\theta v_\theta V_s^2}{r}\frac{\partial B_\theta}{\partial \theta} -$$

$$-[\rho a^2(V_A^2 - V_s^2) - B_\phi^2) + B_r B_\theta V_s v_\theta]\frac{1}{r}\frac{\partial v_\theta}{\partial \theta} -$$

$$-\left[v_\theta(V_A^2 - V_s^2) + \frac{B_r B_\theta V_f}{\rho}\right]\frac{1}{r}\frac{\partial p}{\partial \theta} + \frac{B_\theta v_s^3}{r}\frac{\partial B_r}{\partial \theta} +$$

$$+\frac{v_r V_s^2}{r}[2\rho(V_s^2 - V_A^2) + B_\theta^2] - \frac{V_s^2 B_\theta v_\theta}{r}(B_r + B_\theta \operatorname{ctg}\theta) +$$

$$+\frac{v_\theta V_s^2}{r}[\rho(V_s^2 - V_A^2) - B_\theta^2]\operatorname{ctg}\theta + \frac{v_r v_\theta B_\theta B_r V_s}{r} -$$

$$-\frac{\rho V_s V_\theta^2}{r}(V_A^2 - V_s^2) - \frac{V_s^3 B_\theta^2}{r} + \rho g(V_A^2 - V_s^2)V_s g \,. \tag{A.9}$$

Since the ideal MHD equations have been used, flow is parallel to the magnetic field lines. Thus we determine B_θ from the relation $B_r v_\theta = v_r B_\theta$;

References

Allen, C. W.: 1955, *Astrophysical Quantities*, Cambridge University Press, London.
Guo, W. P., Wang, J. F., Liang, B. X., and Wu, S. T.: 1992, in Z. Švestka, B. V. Jackson, and M. E. Machado (eds.), 'Eruptive Solar Flares', *IAU Symp.* 133, 381.

Hu, Y. Q. and Wu, S. T.: 1984, *J. Comput. Phys.* **55**(1), 33.
Munro, R. J. and Jackson, B. G.: 1977, *Astrophys. J.* **213**, 874.
Nakagawa, Y., Hu, Y. Q., and Wu, S. T.: 1987, *Astron. Astrophys.* **179**, 354.
Parker, E. N.: 1963, *Interplanetary Dynamical Processes*, Interscience, New York.
Pneuman, G. and Kopp, R. A.: 1971, *Solar Phys.* **18**, 258.
Steinolfson, R. S.: 1989, in J. H. Waite, Jr., J. L. Burch, and R. L. Moore (eds.), *Geophys. Monograph* **54**, 269, American Geophysical Union, Washington, D.C.
Steinolfson, R. S.: 1991, *Astrophys. J.* **382**, 677.
Steinolfson, R. S., Suess, S. T., and Wu, S. T.: 1982, *Astrophys. J.* **255**, 730.
Suess, S. T.: 1979, *Space Sci. Rev.* **23**, 159.
Suess, S. T.: 1988, in R. C. Altrock (ed.), *Solar and Stellar Coronal Structure and Dynamics. Proceedings of the 9th Sacramento Peak Summer Symp.*, Sunspot, New Mexico, p. 130.
Suess, S. T., Richter, A. K., Winge, C. R., Jr., and Nerney, S.: 1977, *Astrophys. J.* **217**, 296.
Sun, M. T.: 1991, Ph.Dissertation, University of Alabama in Huntsville.
Wang, A.-H.: 1992, Ph.Dissertation, University of Alabama in Huntsville.